COMET-Projekt 8. Call

D3.2.1 REPORT MATERIAL TESTS AND STRUCTURAL MONITORING DATA

Project title: Railways for Future: Resilient Digital Railway Systems to enhance performance – Area 3.2

Report period: 1.4.2021 – 28.2.2023

Report prepard by (in alphabetical order)
Christian Hellmich (TUW-IMWS), Hermann Höld (TUW-IMWS), Bernd Moritz (ÖBB-Infra), Bernhard Pichler (TUW-IMWS), Wolfgang Obermüller (IGT), Thomas Pilgerstorfer (Geoconsult), Maximilian Sorgner (TUW-IMWS), Ali Razgordanisharahi (TUW-IMWS), Raphael Scharf (TUW-IMWS),

CONTENTS

1 INTRODUCTION

Tunnel engineering is a complex part of modern infrastructure operation. Ensuring the safety and serviceability of tunnels is of paramount importance. Loads imposed on tunnel linings can only be estimated in the design phase., Possibly jeopardizing their integrity, structural monitoring in the construction phase and during operation is crucial for structural health assessment. This report refers to (i) results from innovative material testing of cementitious binders used in tunneling, and (ii) state-of-the-art structural monitoring of both segmental linings used in mechanized tunneling and shotcrete shells used in the New Austrian Tunneling Method.

Section 2 describes a novel method for the characterization of early-age reaction kinetics of cementitious binders, based on the innovative equipment extension of a quasi-isothermal differential calorimeter. Related data provide valuable insight into the dissolution of the cementitious binder into the pore water, and into the precipitation of hydration products from the oversaturated solution. This coupled dissolution-precipitation process drives the mechanical property evolution of (precast as well as sprayed) concrete, the material which constitutes most of the volume of tunnel linings which are exposed to mechanical loads over service periods extending up to 150 years.

Section 3 contains data from material testing: (i) calorimetric data from cementitious binders used in the Koralmtunnel, the Granitztal Tunnel, and the Semmering Base Tunnel, (ii) long-term shrinkage and creep tests on concrete used for the tubbings of the segmental lining of the Koralmtunnel KAT3, (iii) creep tests collected from the scientific literature, and (iv) strength, elasticity, and creep tests performed at early material ages on several Austrian concretes.

Section 4 comprises a collection of data from structural health monitoring of tunnel linings, including (i) data from geodetic displacement measurements of the shotcrete shell of the Tunnel Stein, (ii) data from vibrating wire strain gauges embedded into tubbings of the segmental lining of the Koralmtunnel KAT3, and (iii) monitoring data collected from the literature.

Overall, the present report pays focused attention to the necessity of meticulous monitoring and analysis for ensuring the safety and serviceability of tunnel structures, underscoring the demand for ongoing study in this area, in order to enhance our comprehension and capacity to forecast the behavior of these crucial infrastructure components.

2 DEVELOPMENT AND REALISATION OF A NOVEL MATERIAL TEST: ANALYTICS-BASED QUANTITATIVE CALORIMETRY

Cement hydration in freshly installed NATM-linings frequently implies significant temperature rises, as has been monitored during the advance of the Granitztal tunnel, which with the Koralmtunnel along the Koralmbahn between Graz and Klagenfurt is part of the high-capacity railway corridor linking the Baltic and Adriatic regions. These temperature rises affect the overall thermo-chemo-mechanical behaviour of the lining and its surroundings, which can be elucidated by a coupled analysis method combining the laws of thermodynamics for chemically reactive media with advanced constitutive modelling and structural mechanics. A key material property entering such computations is the heat released per mass of cement and per unit of time during the hydration process. This heat release rate is related to the evolution of the degree of hydration ([1] and [2]), which, in turn, governs important mechanical properties, such as the compressive strength of cement paste and concrete ([3] and [4]). The latter are key input for the thermo-chemo-mechanical analyses of concrete and shotcrete tunnel shells ([5] and [6]).

As part of the Rail4Future project, a novel analytics-based material test was developed and realized to quantitatively determine the heat release rate. This innovative form of calorimetry testing gives access to the instant heat release rate arising from the hydration process.

2.1 Calorimetry and classical estimation of heat release rate

The focus of the present contribution is an improved quantitative evaluation of isothermal calorimetric tests, which we performed by means of an isothermal differential calorimeter of the type ToniCAL Trio 7339, produced by Toni Technik Baustoffprüfsysteme GmbH. From the temperature difference between a hydrating and a chemically inert sample, ΔT, see Figure 1, the total heat flow leaving the hydrating sample, q_{tot}, is determined according to:

$$q_{tot} = CF \cdot \Delta T \qquad (1)$$

whereby the calibration factor CF was determined by a calorimeter-specific calibration test.

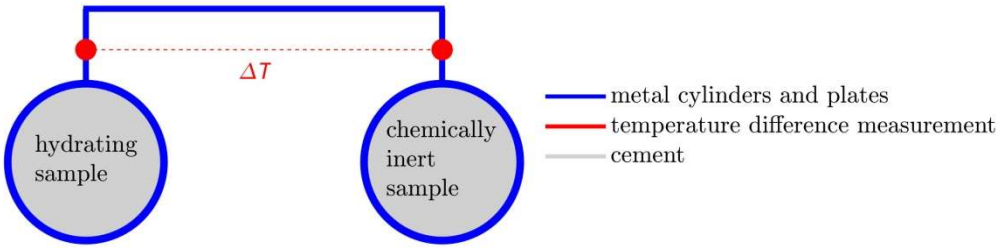

Figure 1: Schematic cross-section of the calorimeter, comprising two metal cylinders hosting a hydrating and an inert sample, respectively, and being thermally connected by metal plates, across which the temperature difference ΔT is measured.

In Figure 2, the total heat flow leaving the hydrating sample, q_{tot}, is shown for a cement paste sample produced with an initial water-to-cement mass ratio of 0.44 and the cement of type CEM I, utilized in the Granitztal tunnel ([7], [8], and [9]). The tested sample, with a height of 55 mm and a radius of b = 8 mm, is depicted in Figure 3.

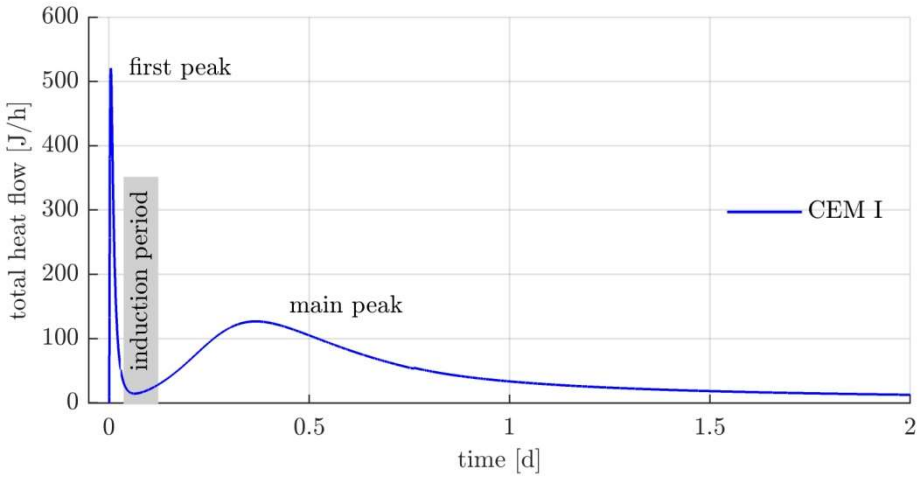

Figure 2: Total heat flow leaving the hydrating sample of the tested CEM I cement utilized in the Granitztal tunnel. The curve is characteristic for cement and shows the first peak, the induction period, and the main peak.

The following typical characteristics of the heat produced by the hydrating sample are observed: A first, high conduction peak, indicating massive heat generation during and right after mixing is followed by a so-called induction period and by a considerably lower and wider main conduction peak. In order to understand the underlying causes of these peaks, Nicoleau and Nonat [10] have conducted a systematic review and evaluation of ion concentration measurements in solutions and hardening cement paste, provided by methods such as inductively coupled plasma (ICP) spectrometry, colorimetry, X-ray diffraction, thermogravimetric analysis (TGA), and calorimetry. They showed that the first peak results from the dissolution process of clinker coming together with an increasing ionic saturation of water ([11]), and that the main peak relates to the coupled dissolution-precipitation process, in which clinker (mainly: tricalcium silicate) is dissolved and calcium-silicate-hydrate and portlandite precipitate ([10]).

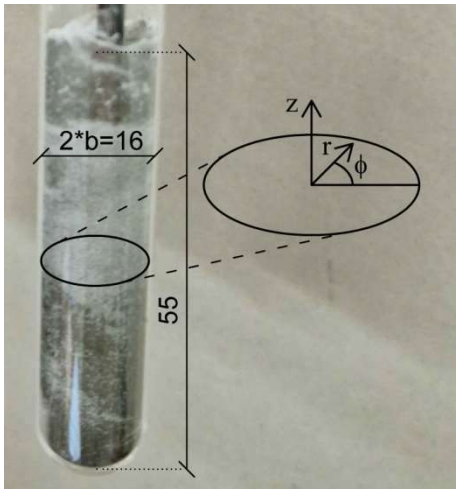

Figure 3: A sample with hardened cement with its cylindrical coordinate system. The dimensions are in millimeters.

The classical estimation of the heat release rate is based on the assumption that the internal energy of the hydrating sample remains constant over the calorimetric test so that the first law of thermodynamics implies the total heat leaving the hydrating sample, as referred to in Eq.(1), to be equal to the heat generation rate of the hydrating sample, g_{tot}, see Figure 2. Accordingly, the division of g_{tot} by the mass of the cement used to produce the sample would approximately result in the specific heat release rate.

2.2 Green's function approach considering instationarity: quantitative determination of heat release rate

For the more accurate quantification of the heat release rate, the change of internal energy is considered; namely in terms of the heat capacity multiplied with the local temperature rise; to be balanced by local heat generation and local heat flux, see also Figure 4. In order to get access to the absolute value of the temperature, rather than to only the temperature difference between the metal cylinders illustrated in Figure 1, an additional temperature sensor was installed in the calorimeter, close to the metal cylinder hosting the hydrating sample.

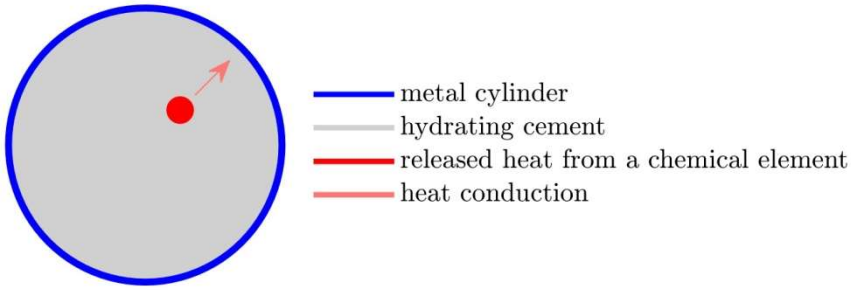

Figure 4: Coupled heat generation-conduction problem in the hydrating sample ([2]): the heat released from material volume ("chemical element") leads to (i) internal energy increase due to local temperature rise, and (ii) heat flow from the material volume to its surrounding.

From a mathematical viewpoint, we resort to the so-called heat conduction equation, which combines the first law of thermodynamics with Fourier's heat conduction law, while restricting internal energy effects to heat capacity phenomena, and we solve the latter for an infinitely long cylinder, with a radial symmetric, uniform distribution of radial heat flow vectors across its outer surface,

$$\boldsymbol{q} = \boldsymbol{e}_{\mathrm{r}} \frac{q_{tot}}{2\pi bh} \,. \tag{2}$$

Under these conditions, the heat conduction equation reads as ([12]):

$$\frac{\partial^2 T}{\partial r^2} + \frac{1}{r}\frac{\partial T}{\partial r} + \frac{g}{k} = \frac{1}{\alpha}\frac{\partial T}{\partial t} \qquad in\ 0 \le r < b, t > 0 \tag{3}$$

$$\begin{aligned} &\text{BC1:} \quad T(r \to 0, t) \to \text{finite} \\ &\text{BC2:} \quad -k\frac{\partial T}{\partial r}(r = b, t) = f(t) \\ &\text{IC:} \quad T(r, t = 0) = F(r) \end{aligned} \tag{4}$$

where $T(r,t)$ is the temperature of the cylinder at position r and time t in °C, b is the radius of the cylinder in m, k is the thermal conductivity in W/mK, $\alpha = k/(\rho c)$ is the thermal diffusivity in m^2/s, ρ is the mass density in kg/m^3, c is the constant volume specific heat in J/(kgK), $F(r)$ is the initial temperature (at time $t = 0$) and $g(r,t)$ is the volumetric rate of internal energy generation in W/m^3. The first boundary condition, BC1, means that the temperature at the axis of the cylinder must have a finite value. The second boundary condition, BC2, specifies the time-varying heat flow $f(t) = q_{tot} / (2\pi bh)$ across the boundary of the sample. The initial condition, IC, will be described later.

Usually, the evolution of the temperature field, $T(r,t)$, is the function to search for in a nonhomogeneous transient heat conduction problem according to the equations (3) and (4). The problem can be solved using Green's functions, and the temperature is calculated as follows ([12]):

$$T(r,t) = \int_{r'=0}^{b} G(r,t|r',\tau=0)F(r')r'\,\mathrm{d}r' \tag{5}$$

$$+ \frac{\alpha}{k} \int_{\tau=0}^{t} G(r,t|b,\tau) f(\tau)\, b \, \mathrm{d}\tau \,,$$

whereby the Green's function reads as:

$$G(r,t|r',\tau) = \frac{2}{b^2} + \frac{2}{b^2} \sum_{n=1}^{\infty} \frac{J_0(\lambda_n r')\, J_0(\lambda_n r)}{J_0^2(\lambda_n b)} e^{-\alpha \lambda_n^2 t} \qquad (6)$$

Usually, equation (5) is used for calculating the temperature in the sample $T(r,t)$. Herein, however, equation (5) is used for calculating the rate of volumetric heat generation $g(r,t)$, which corresponds to the heat release rate per mass g_ρ for a sample containing 10 g of cement through $g_\rho(t) = g_{tot}/(10\ \mathrm{g}) = \int g(r,t)\, dV/(10\ \mathrm{g})$. Evaluation of equation (5) for $r = b$, setting the result equal to the measured temperature evolution, while considering an initially uniform temperature of $F(r) = 25°\mathrm{C}$ and the heat flow $f(t)$ estimated through the measured temperature difference according to equations (1) and (2), allows for estimation of $g(r,t)$, and subsequently, of the heat release rate per unit mass, see Figure 5.

We observe that the heat release peak due to cement dissolution is more than twice as large as classically estimated, and that the latter artificially retards the occurrence of the precipitation peak.

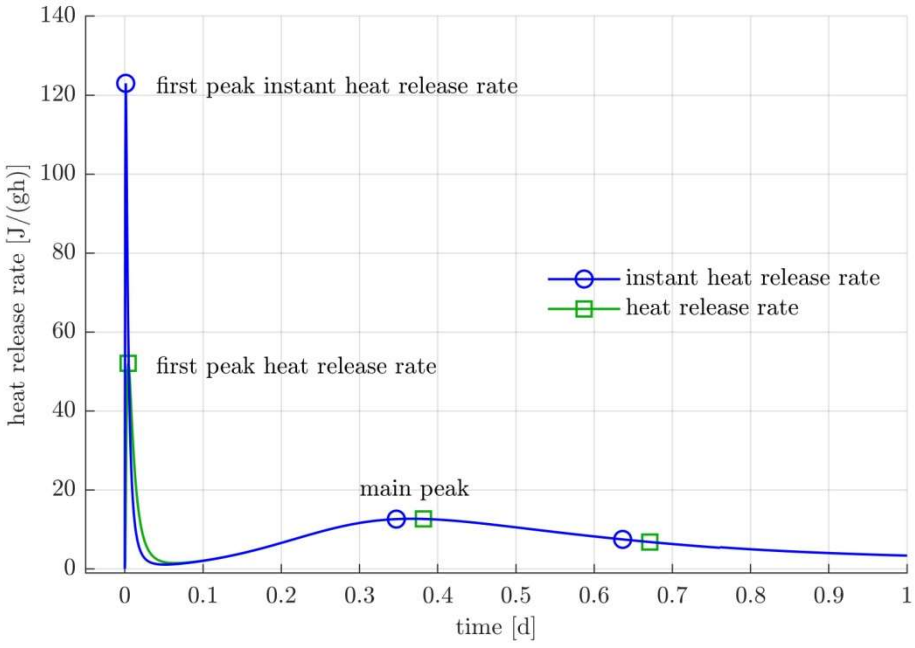

Figure 5: Comparison of the classical estimation of the heat release rate neglecting instationarity and the improved estimation of the heat release rate based on Green's functions of the tested CEM I cement.

Consideration of temperature instationarity resulting from heat capacity effects leads to a higher first heat release peak (due to cement dissolution), and to an earlier occurrence of the second heat peak (due to hydrate precipitation), when compared to the classical estimation method disregarding the aforementioned effects. We

expect this refined representation of the overall hydration process to further enhance the state-of-the-art in the micro-thermo-chemo-mechanics of concrete, as used in NATM tunnel monitoring by so-called hybrid methods ([13]).

3 COLLECTION OF MATERIAL TEST DATA

3.1 Calorimetric test data

A key topic of Area 3.2 is the laboratory characterization of early-age reaction kinetics and the corresponding evolution of the mechanical properties of concrete and shotcrete. The reaction kinetics are described in terms of heat release rates, which are measured with the analytics-based quantitative calorimetry test described in Section 2.2. The calorimetry tests, as part of the work package WP2 "Innovative Testing of Shotcrete and Concrete", are carried out with concretes used in the construction of ÖBB tunnels. These tests are necessary because the analytics-based quantitative calorimetry test has not yet been carried out with these cements, and therefore, no data are available in the literature. The relevant tunnels are the Granitztal Tunnel, the Koralmtunnel, both construction lots KAT2 and KAT3, and the Semmering Base Tunnel, construction lots SBT1.1, SBT2.1 and SBT3.1. Data obtained from material tests of the tunnel concretes are listed in the following sections.

3.1.1 Koralm Tunnel

Table 1: Data of KAT 2 Tübbingbeton (Spezialtübbing Hochfest).

KAT 2 Tübbingbeton (Spezialtübbing Hochfest)			
Number R4F:	1		
Building lot:	Koralmtunnel KAT 2		
Design number:	50571		
Designation:	C50/60/XC4/XA1L/GK16		
Producer:	ARGE KAT2		
Application:	Spetzialtübbing Hochfest, Sohlement Störbereich		
Constituent	**Label**	**Producer**	**TU-Lab**
Cement	CEM II 52,5 N A-S „Der Grüne"	Lafarge Retznei	yes
Additions	FLUAMIX C	Lafarge Retznei	yes
Admixtures	Mapei Advanced 36 (Superplasticizer)	Mapei	no
Aggregates			no
Documents	Erstprüfung		
Calorimetry	Done (cement)		

Table 2: Data of KAT 2 Innenschale Gewölbe bewehrt.

KAT 2 Innenschale Gewölbe bewehrt			
Number R4F:	2		
Building lot:	Koralmtunnel KAT 2		
Annotation:	ATA = aufbereitetes Tunnelmaterial		
Design number:	50162		
Designation:	C25/30(90)/IG/GK22/F59/VV180		
Producer:	ARGE KAT2		
Application:	Innenschale Gewölbe bewehrt – GK22		
Constituent	**Label**	**Producer**	**TU-Lab**
Cement	CEM II 42,5 N A-M „Der Schwarze“	Lafarge Retznei	yes
Additions	FLUAMIX C	Lafarge Retznei	yes
Admixtures	Mapei LSP11 (Superplasticizer)	Mapei	no
Admixtures	CX Isofines + (Superplasticizer)		no
Admixtures	Mapei VZ (Retarder)	Mapei	no
Admixtures	Mapei LP100 (Air entrainment)	Mapei	no
Aggregates			no
Documents	Erstprüfung		
Calorimetry	Scheduled		

Table 3: Data of KAT 3 Tübbingbeton.

KAT 3 Tübbingbeton			
Number R4F:	3		
Building lot:	Koralmtunnel KAT 3		
Design number:	1218		
Designation:	diverse		
Producer:	ARGE PTS KAT 3		
Application:	Tübbinge		
Constituent	**Label**	**Producer**	**TU-Lab**
Cement	CEM II/A-S 52,2 N	w&p Zement GmbH	yes
Additions	Supermic C	w&p Zement GmbH	yes
Admixtures	Premment FT 500 (Superplasticizer)	BT3 Betontechnik	yes
Aggregates	diverse	Jauntaler Kies	no
Documents	Erstprüfung		
Calorimetry	Done		

Table 4: Data of KAT 3 Gewölbebeton Nord.

KAT 3 Gewölbebeton Nord			
Number R4F:	4		
Building lot:	Koralmtunnel KAT 3		
Designation:	C25/30(90)-BS-TU/G-BL-XC3-XF3-C3A-frei-F66-GK22		
Producer:	ARGE PTS KAT 3		
Application:	Innenschale		
Constituent	**Label**	**Producer**	**TU-Lab**
Cement	CEM I 42,5 HS C3A-frei WT27	w&p Zement GmbH	no
Additions	Supermix C	w&p Zement GmbH	yes
Admixtures	dynamIQ flow L-08 (Superplasticizer)	Baustofftechnik	yes
Admixtures	dynamIQ air M-01 (Air entrainment)	Baustofftechnik	yes
Aggregates	diverse	Jauntaler Kies	no
Documents	Erstprüfung		
Calorimetry	Scheduled		

Table 5: Data of KAT 3 Gewölbebeton Süd.

KAT 3 Gewölbebeton Süd			
Number R4F:	5		
Building lot:	Koralmtunnel KAT 3		
Designation:	C25/30(90)-F59-FK22-IG		
Producer:	ARGE Beton KAT 3		
Application:	Innenschale		
Constituent	**Label**	**Producer**	**TU-Lab**
Cement	CEM II/A-M (S, L) 42,5 N WT 38	w&p Zement GmbH	yes
Additions	Supermix C	w&p Zement GmbH	yes
Admixtures	dynamIQ flow L-08 (Superplasticizer)	Baustofftechnik	yes
Admixtures	dynamIQ air M-01 (Air entrainment)	Baustofftechnik	yes
Aggregates	diverse	Jauntaler Kies	no
Documents	Erstprüfung		
Calorimetry	Scheduled		

Table 6: Data of KAT 3 Sohlbeton Süd.

KAT 3 Sohlbeton Süd			
Number R4F:	6		
Building lot:	Koralmtunnel KAT 3		
Designation:	C25/30(90)-F52-GK22-IXAL-B-S		
Producer:	ARGE Beton KAT 3		
Application:	Innenschale		
Constituent	**Label**	**Producer**	**TU-Lab**
Cement	CEM II/A-M (S, L) 42,5 N WT 38	w&p Zement GmbH	yes
Additions	Supermix C	w&p Zement GmbH	yes
Admixtures	dynamIQ flow M-02 (Superplasticizer)	Baustofftechnik	yes
Admixtures	dynamIQ air M-01 (Air entrainment)	Baustofftechnik	yes
Aggregates	diverse	Jauntaler Kies	no
Documents	Erstprüfung		
Calorimetry	Scheduled		

3.1.2 Granitztal Tunnel

Table 7: Data of Granitztaltunnel Anhydritbereich – Außenschale Spritzbeton.

Granitztaltunnel Anhydritbereich – Außenschale Spritzbeton			
Number R4F:	11		
Building lot:	Granitztaltunnel Anhydritbereich		
Designation:	SpC20/25(56)/II/J2/XAT-C3A-frei/GK8/VV4		
Producer:	ATG – Arge Tunnelkette Granitztal Baulos 50.4		
Application:	Außenschale Spritzbeton		
Constituent	**Label**	**Producer**	**TU-Lab**
Cement	CEM I 42,5 R - SR 0 WT 27 C3A-frei	w&p Zement GmbH	yes
Admixtures	Dynamon LZSPW 20 (Superplasticizer)	Mapei	yes
Admixtures	Mapetard VZ M (Retarder)	Mapei	yes
Admixtures	Sigunit L 93 AF (Erstarrungsbeschl.)	Sika	yes
Aggregates	diverse	Sadjak Marco GmbH	no
Documents	Erstprüfung, Identitätsprüfung		
Calorimetry	Done		

Table 8: Data of Granitztaltunnel Anhydritbereich – Innenschale.

Granitztaltunnel Anhydritbereich – Innenschale			
Number R4F:	12		
Building lot:	Granitztaltunnel Anhydritbereich		
Designation:	C30/37(90)G/IXAT-C/F59/GK22		
Producer:	ATG – Arge Tunnelkette Granitztal Baulos 50.4		
Application:	Innenschale (Gewölbe)		
Constituent	**Label**	**Producer**	**TU-Lab**
Cement	CEM I 42,5 R – SR 0 WT 27 C3A-frei	w&p Zement GmbH	yes
Additions	Supermix C	w&p Zement GmbH	yes
Admixtures	Dynamon RC 520 (Superplasticizer)	Mapei	no
Admixtures	Mapeair LP100 (Air entrainment)	Mapei	no
Aggregates	diverse	Sadjak Marco GmbH	no
Documents	Erstprüfung, Identitätsprüfung		
Calorimetry	Done (Cement)		

3.1.3 Semmering Base Tunnel

Table 9: Data of SBT1.1 Spritzbeton.

SBT1.1 Spritzbeton			
Number R4F:	21		
Building lot:	Semmering Basistunnel SBT1.1		
Designation:			
Producer:			
Application:			
Constituent	**Label**	**Producer**	**TU-Lab**
Cement	CEM I 52,5 R	CRH	no
Additions	AHWZ Wopfinger	Wopfinger	no
Admixtures			
Aggregates			
Documents	no		
Calorimetry	Scheduled		

Table 10: Data of SBT1.1 Innenschalenbeton.

SBT1.1 Innenschalenbeton			
Number R4F:	22		
Building lot:	Semmering Basistunnel SBT1.1		
Designation:			
Producer:			
Application:			
Constituent	**Label**	**Producer**	**TU-Lab**
Cement	CEM I 42,5 N SR0 WT27 C3Afrei (Werk Mann.)	Lafarge	yes
Additions	AHWZ Wopfinger	Wopfinger	no
Admixtures			
Aggregates			
Documents	no		
Calorimetry	Scheduled		

Table 11: Data of SBT2.1 Spritzbeton.

SBT2.1 Spritzbeton			
Number R4F:	23		
Building lot:	Semmering Basistunnel SBT2.1		
Designation:			
Producer:			
Application:			
Constituent	**Label**	**Producer**	**TU-Lab**
Cement	CEM I 52,5 R (Werk Mannersdorf) zu 50%	Lafarge	yes
Cement	CEM I 52,5 SP (Werk Retznei) zu 50%	Lafarge	yes
Additions	Fluamix C (Werk Mannersdorf)	Lafarge	yes
Admixtures			
Aggregates			
Documents	no		
Calorimetry	Scheduled		

Table 12: Data of SBT.2.1 Innenschalenbeton.

SBT2.1 Innenschalenbeton			
Number R4F:	24		
Building lot:	Semmering Basistunnel SBT2.1		
Designation:			
Producer:			
Application:			
Constituent	**Label**	**Producer**	**TU-Lab**
Cement	CEM II/A-M (S-L) 42,5 N WT38 "Der Schwarze"	Lafarge	yes
Additions	Fluamix C (Werk Mannersdorf)	Lafarge	yes
Admixtures			
Aggregates			
Documents	no		
Calorimetry	Scheduled		

Table 13: Data of SBT3.1 Spritzbeton.

SBT3.1 Spritzbeton			
Number R4F:	25		
Building lot:	Semmering Basistunnel SBT3.1		
Designation:			
Producer:			
Application:			
Constituent	**Label**	**Producer**	**TU-Lab**
Cement	CEM I 52,5 SP (Werk Retznei)	Lafarge	yes
Additions	Fluamix C (Werk Mannersdorf)	Lafarge	yes
Additions	Dolomix A (Werk SSK)		no
Admixtures			
Aggregates			
Documents	no		
Calorimetry	Scheduled		

Table 14: Data of SBT3.1 Innenschalenbeton.

SBT.3.1 Innenschalenbeton			
Number R4F:	26		
Building lot:	Semmering Basistunnel SBT.3.1		
Designation:			
Producer:			
Application:			
Constituent	**Label**	**Producer**	**TU-Lab**
Cement	CEM II/A-M (S-L) 42,5 N WT38 "Der Schwarze"	Lafarge	yes
Additions	Fluamix C (Werk Mannersdorf)	Lafarge	yes
Admixtures			
Aggregates			
Documents	no		
Calorimetry	Scheduled		

3.2 Long-term creep and shrinkage tests on Koralmtunnel site

In order to analyze the time-dependent viscoelastic material behavior of the concrete used for the production of tubbings of the segmental lining of Koralmtunnel KAT3, shrinkage and creep test were performed in parallel to the production and installation of a measurement ring (Messtübbing Ring 4.292). Six prismatic concrete specimens with a width and a depth of 35 cm, and a height of 70 cm were produced on Dec 5, 2019. Three specimens were used for shrinkage tests (A-C), the remaining three for creep tests (D-F), see Figure 6.

Figure 6: Koralmtunnel KAT3 - Production of specimen for in situ shrinkage and creep tests.

Two vibrating wire strain gauges (Model 4200 series) from GEOKON [14] were embedded close to the center of every specimen, providing measurements of the axial normal strains of the prisms. The sensors are named by the letter of the specimen and by the number of the sensor, e.g. B1 and B2 denote the sensors embedded in the shrinkage test specimen B. The forms were stripped 8 days after casting.

The measurements started one day after production, on Dec 6, 2019. An automatic data logger was used for hourly readings until June 30, 2020. Subsequently, the time interval between two successive readings was increased to 6 hours. The measurements ended after 880 days, on May 4, 2022.

Initially, all specimen were stored in the production hall of the tubbings, near to the segments which became part of the measurement ring (Ring 4.292). Before the start of the creep tests, the specimens were transferred into the tunnel, to cross-passage QS 56. On April 27, 2020, the specimens D, E, and F were loaded by a compressive axial force of 1.235 kN, resulting in a nominal axial compressive normal stress amounting to 10 MPa, see Figure 7. On Sep 28, 2021, the specimens were transferred to Wetterwand Süd.

Figure 7: Koralmtunnel KAT3 - Test setup for in situ creep tests.

Vibrating wire strain gauges are used for measurements of shrinkage and creep strains. Every sensor is equipped with two flanges, holding a wire in a tensile stress state. An electromagnetic coil is used to excite the wire and to measure its natural vibration frequency. Already in its initial reference configuration, the wire is prestressed and vibrates, upon excitation, with a specific eigenfrequency. Several measurements are performed right at the start of the monitoring period, in order to capture the initial reference frequency of every wire. Provided that the distance between the flanges decreases later on, e.g. because the specimen containing the strain gauge is subjected to compression, the tensile prestress of the wire decreases. This results in a reduction of its natural vibration frequency.

As for the evaluation of the shrinkage and creep tests, the measured evolution of the natural frequency of the vibrating wires has to be converted into mechanical strains. The relation between the readings stored in the data logger (= vibration frequencies) and the corresponding axial normal strains is provided in the user manual of the strain gauges (GEOKON Model 4200 series) [14]. Twelve strain evolutions were obtained, two each from specimens A to F, see Figure 8 and Figure 9.

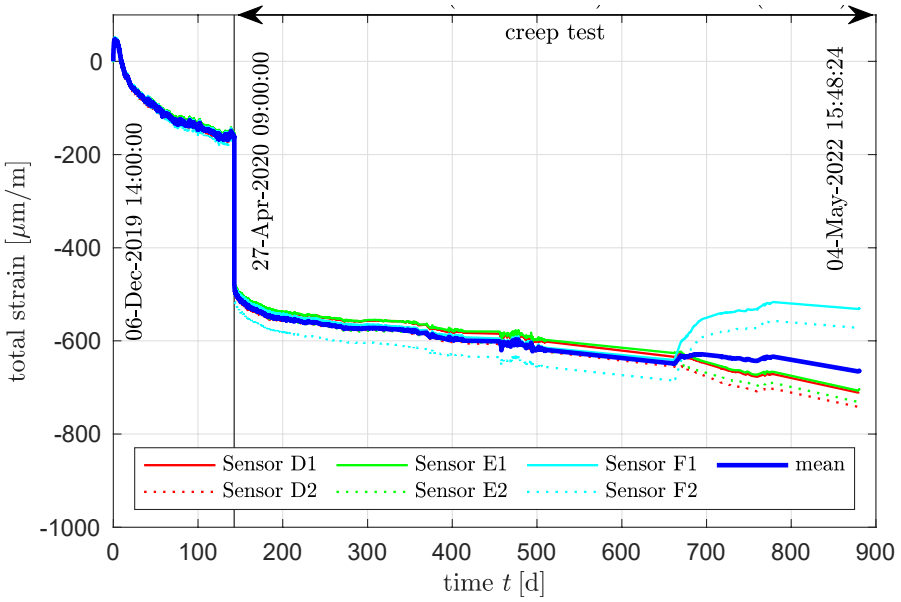

Figure 8: Evolution of axial normal strains measurements in "creep" specimens D, E, and F: the thin solid and dotted lines represent the measurements of two sensors installed in each specimen; the thick blue solid line is the average of all six measurements.

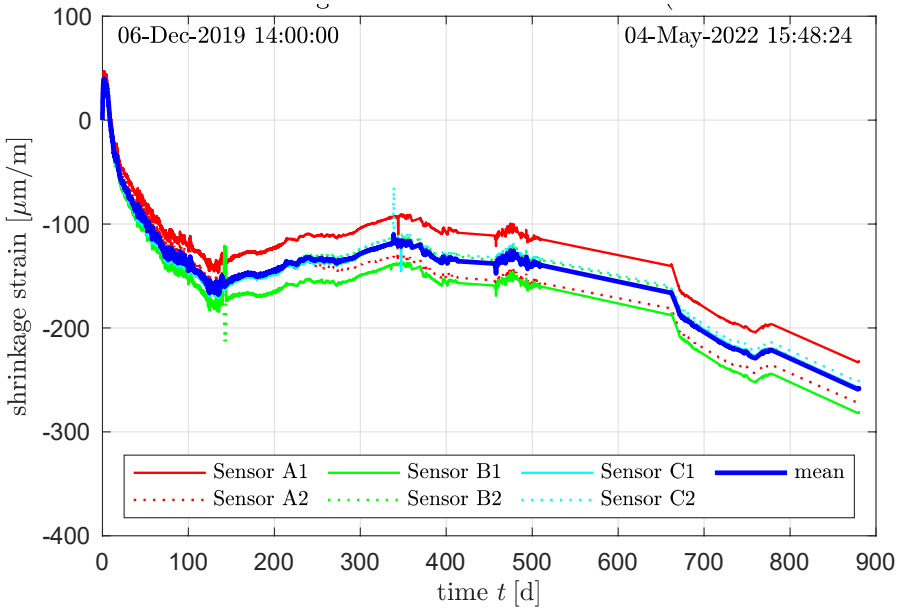

Figure 9: Evolution of axial normal strain measured inside "shrinkage" specimens A, B, and C: the thin solid and dotted lines represent the measurements of two sensors installed in each specimen; the thick blue solid line is the average of all six measurements.

3.3 Collection of creep tests from scientific literature

Creep of concrete is affected by the loading and the environmental conditions: basic creep refers to constant values of both temperature and relative humidity, drying creep refers to a decreasing internal relative humidity, thermal creep to a varying temperature, aging creep to a changing microstructure, and non-linear creep to high stress-levels. A wide range of scientific literature addresses each of these topics individually. A comprehensive database of many different experimental campaigns performed under the mentioned conditions was compiled by Northwestern University and BOKU Wien [15].

In stretches of tunnels which are far away from the portals, the temperature and the relative humidity are virtually constant over time. Therefore, drying and thermal effects are insignificant for the long-term creep of concrete of the lining. Aging creep refers to the situation where the microstructure of concrete changes, e.g. because of ongoing hydration, while the material is exposed to mechanical loads. Thus, aging creep occurs in structures loaded at early material ages, e.g. in shotcrete tunnel shells. As for segmental tunnel linings, in turn, the segments are typically produced a long time before they are put in place in the tunnel. Therefore, aging creep does not play a significant role. Nonlinear creep is the name given to the amplification of the creep activity of concrete, which results from increased compressive stress levels. This phenomenon is governed by the degree of utilization, which is equal to the imposed stress, σ, divided by the compressive strength of concrete, f_c. Nonlinear creep becomes significant for stresses exceeding some 40% of the compressive strength.

Creep of concrete significantly influences the long-term behavior of tunnel linings which in case of OeBB tunnels shall remain in service for up to 150 years. Data from creep tests with a duration of several years are very valuable for the calibration of long-term creep models. This provided the motivation to screen the database [15] for long-term basic creep tests, performed at a constant temperature (T) and a constant relative humidity (RH), see Table 15.

Table 15: Essential information of creep test data from scientific literature.

Name	Cement type	year	Ref.	t_0 [d]	W/C [-]	RH [%]	T [°C]	$f_{c,28d}$ [MPa]	σ [MPa]	$\sigma / f_{c,28d}$ [-]
Concrete										
Browne		**1969**	[16]	28 60 400	0.42	100	20			
Kommendant	Type II (Medusa)	**1976**	[17]	28 90 270	0.38	99	20	45.0	14.5	0.32
Li	OPC 42.5	**2021**	[18]	28	0.35	50	20	55.9	13.5	0.24
Rostasy	-	**1973**	[19]	28	0.41	95	20	41.0	9.3	0.23
Theiner	CEM II 42.5N	**2017**	[20]	28	0.44	65	20	35.9	10.8	0.3
Rossi et al.	CEM I 52.5 N	**2012**	[21]	266	0.54	95	20	46	24.4-36.8	0.54-0.80
Rossi et al.	CEM I 52.5 N	**2013**	[22]	28 145 145	0.54	95	20	39.9 48.6 48.6	13.6 24.7 33	0.34 0.51 0.68
Cement										
Zhang	Saint Vigor (0SV)	**2014**	[23]	28	0.50	50	20	-	9.4	ca. 0.28
	Saint Vigor (0SV)				0.38			-	15.6	0.13-0.22
	Saint Vigor (1SV)				0.38					
	Saint Vigor (0SV)				0.28					
	Saint Vigor (1SV)				0.28					
	Saint-Pierre-la-Cour				0.38					

3.4 Strength-, elasticity-, and creep-evolution of shotcrete and precast segmental linings: collection from scientific literature

For the purposes of concrete engineering, codes of practice describe the early-age evolution of the uniaxial compressive strength and the modulus of elasticity of isothermally curing concrete by empirical exponential functions [24]. Properties of a specific concrete of interest are accounted for by means of the specific 28 days value of the uniaxial compressive strength, $f_{c,28d}$, and dimensionless parameters s and α, accounting for the specific types of cement and aggregates used to produce the concrete, see

Table 18. These functions were extended in [25], so as to include the early-age evolution of the creep modulus. In addition, the functions provided in [24] were tested based on results of standard and innovative early-age strength and stiffness testing of concretes, see Table 19. Whenever necessary, improved values of *s* were determined, see Table 16 and Table 17.

Table 16: Data-driven optimal dimensionless parameter s [25].*

Cement	Aggregate	s_{fc}	s_E	s^*
CEM II/A-M (S-L) 42.5 N	quartz	0.23/0.24	0.20/0.19	0.22
	limestone	0.22/0.25	0.23/0.23	
CEM II/A-S 42.5 R	quartz	0.17/0.16	0.15/0.18	0.18
	limestone	0.16/0.19	0.20/0.19	
CEM I 52.5 R	quartz	0.08/0.09	0.11/0.09	0.09
	limestone	0.05/0.09	0.11/0.11	

Table 17: Data-driven optimal dimensionless parameters s^*_{Ec} [25].

Cement	Aggregates	s_{Ec}	s^*_{Ec}
CEM II/A-M (S-L) 42.5 N	quartzite	0.65/0.67/0.60/0.54	0.62
	limestone	0.64/0.66/0.60/0.59	
CEM II/A-S 42.5 R	quartzite	0.63/0.60/0.63/0.57	0.61
	limestone	0.63/0.61/0.65/0.54	
CEM I 52.5 R	quartzite	0.53/0.40/0.50/0.48	0.5
	limestone	0.54/0.55/0.58/0.45	

Table 18: Dimensionless parameters s and α suggested by the fib Model Code 2010 [24].

$f_{c,28d}$	Cement Type	s	Aggregate Type	α
≤60 MPa	32.5 N	0.38	basalt, dense limestone	1.2
≤60 MPa	32.5 R, 42.5 N	0.25	quartz	1
≤60 MPa	42.5 R, 52.5 N, 52.5 R	0.2	limestone	0.9
>60 MPa	all classes	0.2	sandstone	0.7

Table 19: Determined properties of one cubic meter of concrete, based on its ingredient mixture [25].

Concrete Type	Cement Type	Aggregate Type	w/b (-)	Water (kg)	Agg. (kg)	Cem. (kg)	SCM (kg)	AEA (kg)	SP (kg)
C30/37/W55	CEM II/	quartz	0.48	170	1832	320	40	0.13–6.05	3.78
3-10B5/GK22/F52	A-M(S-L) 42.5 N	limestone	0.48	170	1875	320	40	0.10–4.70	4.42
C35/45	CEM II/	quartz	0.45	185	1755	410	-	1.03–7.59	0.62
3-10 B5/GK22/F52	A-S 42.5 R	limestone	0.45	185	1796	410	-	0.21–5.08	0.16
C40/50	CEM I/	quartz	0.42	175	1773	420	-	0.13-3.53	1.13
3-10 B5/GK22/F52	52.5 R	limestone	0.42	175	1814	420	-	0.17–5.84	6.17

4 COLLECTION OF STRUCTURAL MONITORING DATA

4.1 Data from geodetic measurements

Structural monitoring of tunnel linings is essential because, unlike in other branches of civil engineering, in tunnel engineering the load acting on the linings can only be estimated *a priori*. For this reason, shotcrete shells, as used in the New Austrian Tunneling Method, are equipped with measurement cross-sections, where at selected points (measuring points MP*i*) on the inner surface of the tunnel shell, 3D displacement vectors are quantified by means of geodetic measurements, in order to be able to subsequently monitor the tunnel shell by means of hybrid methods. Nowadays, up to five MP*i* are provided for a measurement cross-section in the top heading, and one additional MP*i* per bench, see Figure 10.

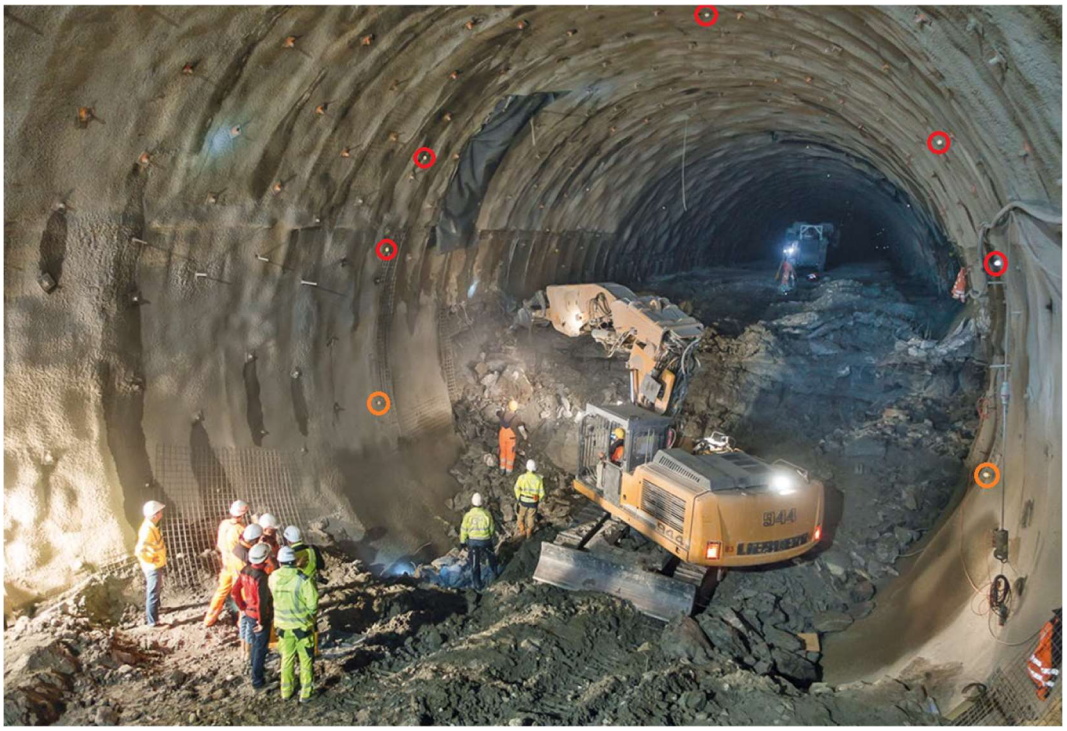

Figure 10: Bench excavation in Stein Tunnel: Measurement cross-section with the five measurement points of the top heading (5 MPi, red), and with one measurement point per bench (2 MPi, orange) (Photo: ÖBB/Moraus) [26].

Geodetic measurements are carried out in tunnel engineering during construction and long-term service. The measurements are carried out using a total station (tachymeter) and targets, see Figure 11. During construction, the displacements are measured once every day. For the targets, precise prism targets as well as bireflex targets (reflectors) are used. They are typically placed on concreted threaded supports in the shotcrete of the outer shell. Regarding the documentation, the individual points are usually designated with a two-part number: the first part describes the stationing of the measurement cross-section and the second part provides information about the location of the point in the cross-section itself.

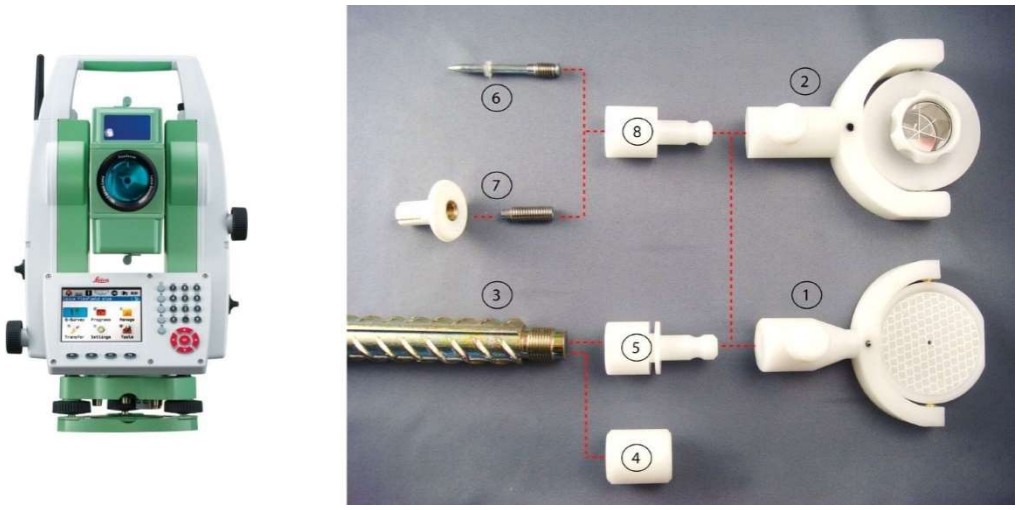

Figure 11: Tachymeter (example Leica, TS 09) and components of 3D displacement monitoring targets [27].

Complete monitoring requires a networked observation scheme that is established with several reference points, see Figure 12. Free stationing is used as a common method for establishing new (measurement) positions, where the past stable bench or invert points are assumed to be fixed points, see also Figure 12.

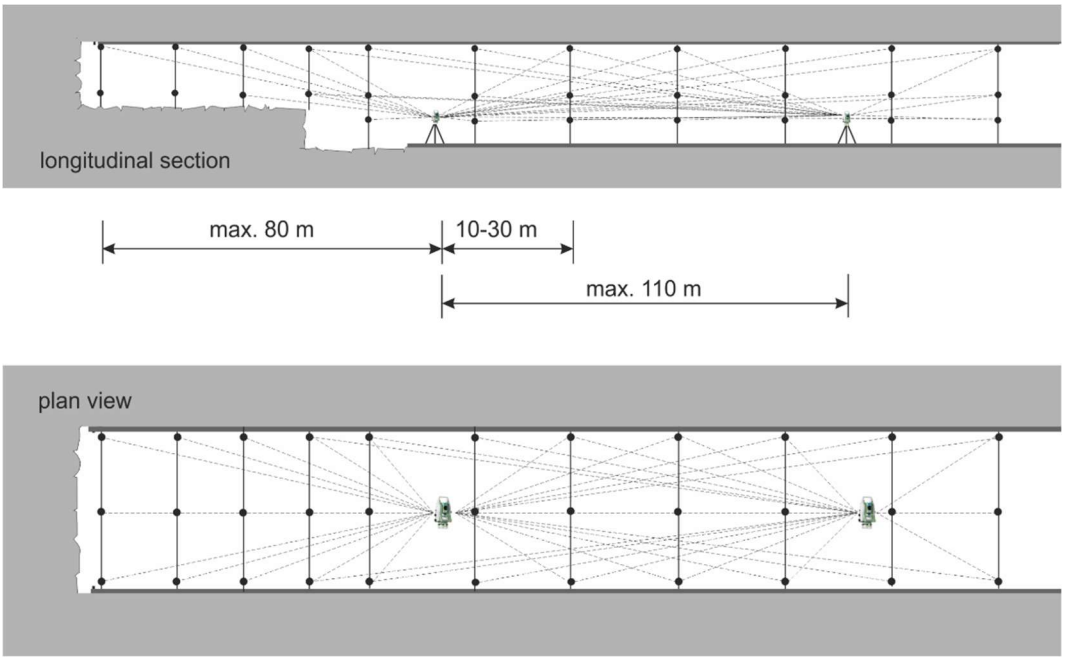

Figure 12: Sketch of an interlinked free station method in the tunnel [27].

Also at the *tunnel Stein*, which is one of the six tunnels of the tunnel *chain St. Kanzian*, which is part of the *Koralmbahn* between *Graz* and *Klagenfurt*, 3D displacement vectors were measured as part of structural monitoring during construction. During the excavation and installation phase of the top heading, the measurement cross section *MQ000201* was equipped with five optical reflectors (measurement points MP1, MP2, MP3, MP4, and MP5), at which 3D displacement vectors were measured;

and the corresponding data set of these measured 3D displacements, from the said measurement cross-section, was provided to the *Institute for Mechanics of Materials and Structures*, *TU Wien*, by *IGT Geotechnik und Tunnelbau Ziviltechniker GmbH*. The displacement measurements in vertical and horizontal direction are listed in Table 20 and

Table 21.

Table 20: Cartesian components of measured displacement vectors of the three measurement points (MP) of measurement cross section MQ000201 of Tunnel Stein.

Measurement data of MP1-MP3									
Zeitpunkt [d]	uxMP1 [m]	uyMP1 [m]	uzMP1 [m]	uxMP2 [m]	uyMP2 [m]	uzMP2 [m]	uxMP3 [m]	uyMP3 [m]	uzMP3 [m]
0,00	0,00000	0,00000	0,00000	0,00000	0,00000	0,00000	0,00000	0,00000	0,00000
1,00	-0,00081	-0,00231	-0,00049	-0,00135	-0,00285	-0,00014	0,00006	-0,00106	0,00003
1,92	-0,00701	-0,01181	-0,00169	-0,00945	-0,01225	-0,00114	-0,00054	-0,00876	0,00113
2,96	-0,00831	-0,01781	-0,00399	-0,01105	-0,01825	-0,00274	-0,00104	-0,01296	0,00073
4,04	-0,00771	-0,02171	-0,00409	-0,01165	-0,02095	-0,00174	-0,00114	-0,01676	0,00113
6,04	-0,00701	-0,02301	-0,00429	-0,01075	-0,02235	-0,00244	-0,00074	-0,01826	0,00113
6,92	-0,00761	-0,02311	-0,00439	-0,01135	-0,02325	-0,00204	-0,00014	-0,01946	0,00163
7,96	-0,00771	-0,02501	-0,00429	-0,01145	-0,02395	-0,00164	0,00106	-0,02076	0,00173
8,92	-0,00691	-0,02371	-0,00379	-0,01105	-0,02325	-0,00104	-0,00034	-0,01966	0,00273
9,96	-0,00691	-0,02441	-0,00369	-0,01135	-0,02345	-0,00074	0,00006	-0,02106	0,00263
10,92	-0,00681	-0,02601	-0,00409	-0,01075	-0,02545	-0,00154	-0,00004	-0,02236	0,00293
11,92	-0,00791	-0,02431	-0,00489	-0,01075	-0,02395	-0,00254	-0,00094	-0,02056	0,00133
13,21	-0,00721	-0,02181	-0,00279	-0,01085	-0,02395	-0,00154	-0,00044	-0,02156	0,00303
14,00	-0,00811	-0,02341	-0,00369	-0,01215	-0,02395	-0,00174	-0,00104	-0,02156	0,00183
14,92	-0,00671	-0,02401	-0,00569	-0,01075	-0,02445	-0,00224	-0,00014	-0,02236	0,00223
15,88	-0,00681	-0,02731	-0,00449	-0,01125	-0,02415	-0,00214	0,00036	-0,02236	0,00193
17,08	-0,00691	-0,02511	-0,00349	-0,01045	-0,02495	-0,00184	0,00036	-0,02206	0,00313
17,92	-0,00701	-0,02591	-0,00399	-0,01035	-0,02505	-0,00084	0,00016	-0,02196	0,00373
19,00	-0,00741	-0,02541	-0,00399	-0,01035	-0,02515	-0,00224	0,00046	-0,02216	0,00293
20,04	-0,00651	-0,02591	-0,00369	-0,00995	-0,02595	-0,00274	0,00126	-0,02296	0,00413
20,96	-0,00671	-0,02591	-0,00379	-0,01085	-0,02615	0,00016	0,00006	-0,02306	0,00363
22,04	-0,00561	-0,02471	-0,00409	-0,00985	-0,02765	0,00006	0,00116	-0,02316	0,00363
23,00	-0,00721	-0,02611	-0,00319	-0,01095	-0,02565	0,00066	0,00026	-0,02386	0,00503
23,96	-0,00681	-0,02661	-0,00429	-0,01075	-0,02685	-0,00014	0,00076	-0,02406	0,00433
39,96	-0,00701	-0,02551	-0,00289	-0,01155	-0,02565	-0,00044	0,00046	-0,02366	0,00393

Table 21: Cartesian components of measured displacement vectors of the two measurement points (MP) of measurement cross section MQ000201 of Tunnel Stein.

Measurement data of MP4-MP5						
Zeitpunkt [d]	uxMP4 [m]	uyMP4 [m]	uzMP4 [m]	uxMP5 [m]	uyMP5 [m]	uzMP5 [m]
0,00	0,00000	0,00000	0,00000	0,00000	0,00000	0,00000
1,00	0,00080	-0,00209	-0,00010	0,00068	-0,00186	-0,00024
1,92	0,00160	-0,00989	-0,00010	0,00578	-0,01036	-0,00254
2,96	0,00200	-0,01509	-0,00060	0,00558	-0,01496	-0,00414
4,04	0,00170	-0,01739	-0,00020	0,00658	-0,01826	-0,00524

6,04	0,00130	-0,01869	-0,00050	0,00608	-0,01956	-0,00594
6,92	0,00200	-0,01939	0,00000	0,00658	-0,01936	-0,00574
7,96	0,00270	-0,02189	0,00090	0,00738	-0,02146	-0,00564
8,92	0,00150	-0,02009	0,00100	0,00628	-0,02016	-0,00564
9,96	0,00210	-0,01999	0,00130	0,00648	-0,02046	-0,00474
10,92	0,00240	-0,02249	-0,00020	0,00708	-0,02166	-0,00504
11,92	0,00260	-0,02139	0,00010	0,00698	-0,01986	-0,00284
13,21	0,00290	-0,02119	0,00120	0,00568	-0,01916	-0,00404
14,00	0,00110	-0,02149	0,00030	0,00568	-0,02076	-0,00534
14,92	0,00180	-0,02169	0,00020	0,00638	-0,02126	-0,00524
15,88	0,00230	-0,02209	0,00060	0,00588	-0,02336	-0,00524
17,08	0,00270	-0,02189	0,00060	0,00608	-0,02176	-0,00464
17,92	0,00280	-0,02209	0,00040	0,00588	-0,02226	-0,00454
19,00	0,00300	-0,02239	0,00090	0,00578	-0,02186	-0,00414
20,04	0,00420	-0,02299	0,00190	0,00618	-0,02216	-0,00424
20,96	0,00290	-0,02289	0,00000	0,00568	-0,02236	-0,00454
22,04	0,00380	-0,02289	-0,00060	0,00618	-0,02236	-0,00474
23,00	0,00310	-0,02319	0,00110	0,00548	-0,02186	-0,00354
23,96	0,00310	-0,02359	0,00070	0,00568	-0,02226	-0,00364
39,96	0,00330	-0,02309	0,00080	0,00568	-0,02186	-0,00364

The geometric data of the measurement cross-section is provided in Table 22. The radius of the tunnel shell amounts to 6.18 m, its thickness to 0.30 m, and its opening angle to 158.98°. As for the positions of the measurement points see also Table 22.

Table 22: Additional data regarding the measurement cross-section MQ000201 of Tunnel Stein

Material und geometrical data		
Baustelle:	Tunnel Stein (Tunnelkette: St. Kanzian)	
Betonsorte:	SpC25/30	
Öffnungswinkel:	158,98	[Grad]
Schalenradius:	6,18	[m]
Schalendicke:	0,3	[m]
Position vom MP1:	11,91	[Grad]
Position vom MP2:	38,55	[Grad]
Position vom MP3:	81,2	[Grad]
Position vom MP4:	140,92	[Grad]
Position vom MP5:	170,89	[Grad]
(ausgehend von der Horizontalen)		

The available geometric data and displacement measurements will be combined with theoretically well-founded concepts of material and structural mechanics, such as to enable a hybrid structural analysis approach which rests on closed-form mathematical formulations. This will allow for the analytical conversion of discrete displacement measurements into continuous displacement and deformation fields, the conversion of the latter into stresses experienced by shotcrete, the quantification of its degree of utilization, and the estimation of external forces acting on the tunnel shell, i.e., ground pressure and impost forces.

4.2 Data from vibrating wire strain sensors

The collection of structural monitoring data is an essential prerequisite for the assessment of the safety and performance of underground structures such as tunnels. In this following, we focus on the monitoring data collected from vibrating wire strain sensors mounded at specific positions to the steel reinforcements embedded in the tubbings of specific segmental lining rings of the Koralmtunnel KAT3. The tunnel lining has an inner diameter of 8.80 m and consists of seven segments per ring, with six segments having an opening angle of 55.385 degrees and the keystone segment having an opening angle of 27.69 degrees. The radial thickness and axial length of each segment are 0.35 m and 1.90 m, respectively. The annular gap between the segmental tunnel ring and the groundmass was filled with a cementitious grout, as indicated in Figure 13.

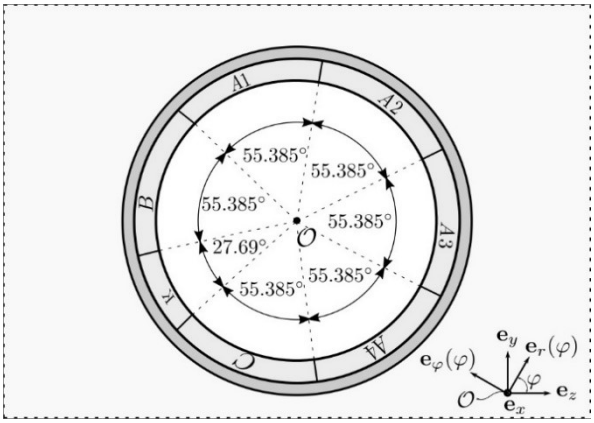

Figure 13: Arrangement of seven tubbings constituting one segmental lining ring of the Koralmtunnel KAT3.

To measure the evolution of circumferential normal strains, vibrating wire strain sensors were attached to circumferential reinforcement bars, as shown in Figure 14. Each tubbing (except for the keystone) was equipped with six strain sensors, with three sensors each attached to the outer and inner circumferential reinforcements, providing representative insight into the deformation of the tubbings at angular positions referred to as φ_1, φ_2, and φ_3, as illustrated as red dots in Figure 15.

Figure 14: Vibrating wire strain sensors mounted to reinforcement bars of tubbing, prior to placement of concrete (copyright Ernst & Sohn GmbH. Reproduced with permission) [28].

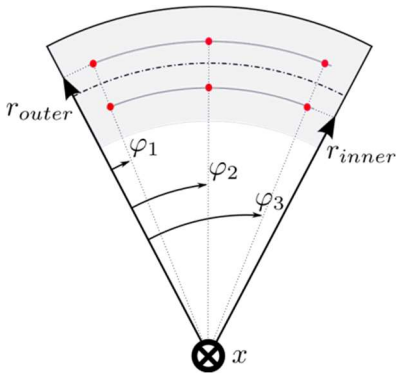

Figure 15: Locations of six strain gauges, see the red dots, inside the segments A1, A2, A3, A4, B, and C shown in Figure 13.

Data from vibrating wire strain sensors installed in three different segmental tunnel rings are available, see Table 23.

Table 23: Number of monitored segmental tunnel rings and format of data provided.

Ring Number	
2013	Strain History (CSV and Excel)
1915	Strain History (CSV)
4292	Strain History (CSV)

These monitoring data serve as input for a data-informed structural analysis model which is based on closed-form mathematical formulations. The model is capable of quantifying and extrapolating the utilization degree of concrete. It is planned to use the monitoring data also used to estimate the ground shear and ground pressure acting on the tunnel lining. The combination of data from both material testing and structural monitoring allows for the elaboration of a comprehensive understanding of the behavior of the segmental tunnel lining of KAT3 and, therefore, contributes to its safe and continuous operation.

4.3 Monitoring data collection from scientific literature

As for validation of our research results, a comprehensive set of monitoring data was collected from the scientific literature. The collected data was obtained with different types of measurement methods. The latest published measurement data include, e.g. fiber optic measurements of circumferential normal strains inside four different rings of the segmental lining of the Suzhou metro, collected during the first five months after installation, see Figure 16.

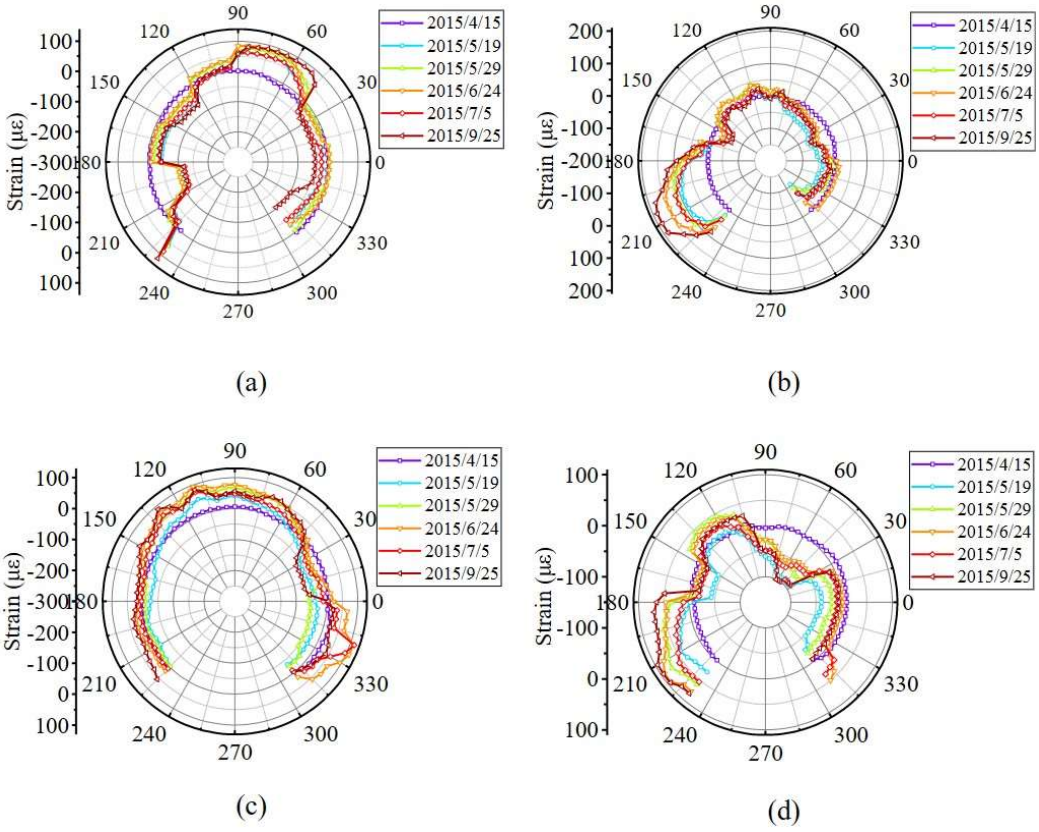

Figure 16: Circumferential normal strains distributions at six different time instants of four different rings of the Suzhou metro station, measured by means of embedded fiber optic sensors [29].

Another valuable data source refers to a segmented tunnel in Belgium. Strain gauges and laser optics were used to record the strains and displacements, respectively, of three adjacent segments. These data provide insight into the important question of segment-to-segment interaction. The displacement determined by means of laser scanning provide insight into the ovalisation of the initially circular tunnel ring, see Figure 17. The described sets of monitoring data complement the data provided by ÖBB.

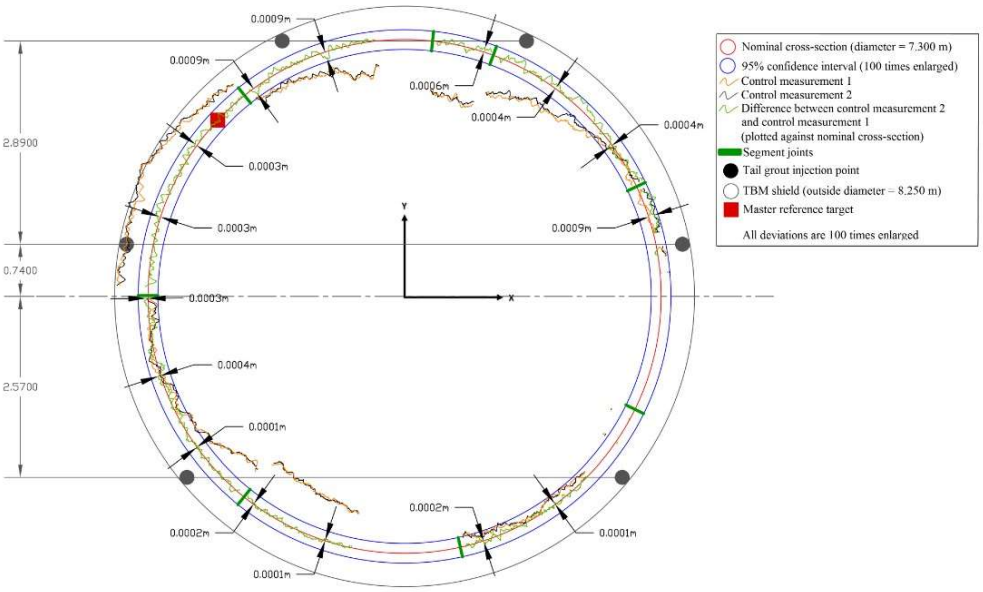

Figure 17: Graphical representation of the undeformed and a deformed configuration of a segmental tunnel ring: surface displacements were quantified by means of the laser scanner method [30].

5 OUTLOOK

Testing with the innovatively equipped quasi-isothermal differential calorimeter are being continued to characterize more cements used in ÖBB-tunnels. In order to further increase the number of experiments which can be performed within the Rail4Future project, a student was found who is performing additional tests as part of his bachelor thesis. All these tests provide quantitative insight into the early-age reaction kinetics of cementitious binders used for tunnel linings. The collected data provide valuable input for analytical and semi-analytical multiscale material modelling of shotcrete and concrete, which is aimed at bridging (i) the spatial scales from microscopic hydration products up to macroscopic representative volume elements of concrete and shotcrete, and (ii) the temporal scales from early-age hardening to long-term creep during structural service life extending to 150 years for OeBB tunnels.

In order to describe the long-term behavior of concrete tunnels up to 150 years, a basic creep model will be developed and calibrated using experimental data from Koralmtunnel KAT3 and the scientific literature [16, 17, 18, 19, 20]. In addition, the effect of stress levels exceeding 40% of the uniaxial compressive strength of concrete on the creep activity of the material will be investigated. A model will be elaborated based on the test results published by Rossi et al. [21, 22]. These creep models will be made ready for use in structural analysis of segmented concrete linings.

Quantification of degrees of utilization of shotcrete shells installed in the New Austrian Tunneling Method will be supported by the described geodetic displacement measurements, geometric data of the monitored tunnel shell, and the evolution of the material properties of the used shotcrete. Structural analysis will cover both the construction phase and the service life, with the aim to compute long-term predictions of load levels experienced by shotcrete. Additional displacement measurements of other measurement cross-sections would be useful for the continuous refinement of the developed structural model, and for extending the scope of the analysis from one measurement cross-section to entire tunnel sections. Additional information regarding geological conditions and the construction process, such as cut lengths, anchor placements, history of bench and invert excavation as well as corresponding shell construction, are desirable for the validation of results from structural analyses.

6 REFERENCES

[1] F.-J. Ulm, O. Coussy, „Strength growth as chemo-plastic hardening in early age concrete," *Journal of Engineering Mechanics, 122(12),* p. 1123–1132, 1996.

[2] C. Hellmich, F.-J. Ulm, H. Mang, „Consistent linearization in Finite Element analysis of coupled chemo-thermal problems with exo- or endothermal reactions," *Computational Mechanics, 24,* p. 238–244, 1999.

[3] B. Pichler, C. Hellmich, „Upscaling quasi-brittle strength of cement paste and mortar: A multi-scale engineering mechanics model," *Cement and Concrete Research, 41,* p. 467–476, 2011.

[4] M. Königsberger, M. Hlobil, B. Delsaute, S. Staquet, C. Hellmich, B. Pichler, „Hydrate failure in ITZ governs concrete strength: A micro-to-macro validated engineering mechanics model," *Cement and Concrete Research, 103,* p. 77–94, 2018.

[5] C. Hellmich, H. Mang, F.-J. Ulm, „Hybrid method for quantification of stress states in shotcrete tunnel shells: combination of 3D in situ displacement measurements and thermochemoplastic material law," *Computers & Structures, 79 (22),* p. 2103–2115, 2001.

[6] R. Scharf, B. Pichler, R. Heissenberger, B. Moritz, C. Hellmich, „Data-driven analytical mechanics of aging viscoelastic shotcrete tunnel shells," *Acta Mechanica,* p. 2989–3019, 2022.

[7] J. Bauer, B. Kohlböck, B. Moritz, G. Zwittnig, „The Granitztal tunnel chain - state of works on the second longest tunnel system on the Koralmbahn / Tunnelkette Granitztal – Stand der Arbeiten für das zweitlängste Tunnelsystem an der Koralmbahn," *Geomechanics and Tunnelling, 9 (5),* p. 416–427, 2016.

[8] G. Gschwandtner, U. Kahn, B. Kohlböck, B. Moritz, S. Wagner, „Granitztal tunnel chain - Experience from the construction of the Langer Berg Tunnel and challenges in the anhydrite zone," *Geomechanics and Tunnelling, 10 (6),* p. 730–73, 2017.

[9] B. Moritz, R. Heissenberger, T. Schachinger, W. Lienhart, „Long-term monitoring of railway tunnels," *Geomechanics and Tunnelling, 14 (1),* p. 35–46, 2021.

[10] L. Nicoleau, A. Nonat, „A new view on the kinetics of tricalcium silicate hydration," *Cement and Concrete Research, 86,* p. 1–11, 2016.

[11] L. Nicoleau, A. Nonat, D. Perrey, „The di- and tricalcium silicate dissolutions," *Cement and Concrete Research, 47,* p. 14–30, 2013.

[12] D. Hahn, M. Özişik, Heat Conduction, 3rd Edition, John Wiley & Sons, Inc., 2012.

[13] B. Pichler, C. Hellmich, „Hybrid methods for shotcrete and segmental linings tunnel shells – combining displacement and rotation measurements with computational multiscale mechanics," *Geomechanics and Tunnelling, 11 (3),* p. 226–235, 2018.

[14] GEOKON, „Model 4200 Series - Vibrating Wire Strain Gauges - Instruction Manual," 2019.

[15] „BOKU," 24 09 2018. [Online]. Available at: https://boku.ac.at/en/baunat/cd-labor/downloads/kriechen-und-schwinden. [last access: 22 03 2023].

[16] R. Browne, R. Blundell, „The influence of loading age and temperature on the long term creep behavior of concrete in a sealed, moisture stable, state," *Matériaux et Construction,* 2, p. 133–143, 1969.

[17] Z. P. Bazant, J.-K. Kim, „Improved prediction model for time-dependent deformations of concrete: Part 2 - Basic creep," *Materials and Structures,* 24, p. 409–421, 1991.

[18] Y. Li, Y. Liu, Y. Li, Y. Li, R. Wang, „Evaluation of concrete creep properties based on indentation test and multiscale homogenization method," *Cement and Concrete Composites,* 123, p. 104135, 2021.

[19] F. Rostásy, K.-T. Teichen, H. Engelke, „Beitrag zur Klärung des Zusammenhanges von Kriechen und Relaxation bei Normalbeton," *SCHRIFTENR OTTO-GRAF-INST,* 57, 1973.

[20] Y. Theiner, M. Drexel, M. Neuner, G. Hofstetter, „Comprehensive study of concrete creep, shrinkage and water content evolution under sealed and drying conditions," *Strain,* 53, p. e12223, 2017.

[21] P. Rossi, J. Tailhan, F. Le Maou, „Creep strain versus residual strain of a concrete loaded under various levels of compressive stress," *Cement and Concrete Research,* 51, pp. 32–37, 2013.

[22] P. Rossi, J. Tailhan, F. Le Maou, L. Gaillet, E. Martin, „Basic creep behavior of concretes investigation of the physical mechanisms by using acoustic emission," *Cement and Concrete Research,* 42, p. 61–73, 2012.

[23] Q. Zhang, R. Le Roy, M. Vandamme, B. Zuber, „Long-term creep properties of cementitious materials: Comparing microindentation testing with macroscopic uniaxial compressive testing," *Cement and Concrete Research,* 58, p. 89–98, 2014.

[24] L. Taerwe, S. Matthys, et al., *fib Model Code for concrete structures 2010,* Ernst & Sohn, Wiley, 2013.

[25] M. Ausweger, E. Binder, O. Lahayne, R. Reihsner, G. Maier, M. Peyerl, B. Pichler, „Early-age evolution of strength, stiffness, and non-aging creep of concretes: Experimental characterization and correlation analysis," *Materials,* 12(2), p. 207, 2019.

[26] T. Herzeg, T. Moraus, „St. Kanzian tunnel chain – Current state of works," *Geomechanics and Tunnelling, 10,* p. 740–747, 2017.

[27] OeGG, „Austrian Society for Geomechanics: Handbook for geotechnical monitoring in conventional tunnelling," 2014.

[28] N. Radončić, K. Martin, W. Martin, B. Moritz, „Strain gauges in pre-cast concrete segments," *Geomechanics and Tunnelling,* 3(8), p. 256–272, 2015.

[29] H.-H. Zhu, D.-Y. Wang, B. Shi, X. Wang, G.-Q. Wei, „Performance monitoring of a curved shield tunnel during adjacent excavations using a fiber optic nervous sensing system," *Tunnelling and Underground Space Technology,* 124, p. 104483, 2022.

[30] K. Schotte, „Verification of the Performance of Segmental Tunnel Linings Using Strain and Ovalisation Monitoring," Ghent University, Faculty of Engineering and Architecture, 2016.